Journal of Power Sources 266 (2014) 365–373

Contents lists available at ScienceDirect

Journal of Power Sources

journal homepage: www.elsevier.com/locate/jpowsour

Synthesis and characterization of 3D Ni nanoparticle/carbon nanotube cathodes for hydrogen evolution in alkaline electrolyte

M.A. McArthur [a, b, *], L. Jorge [a], S. Coulombe [a], S. Omanovic [b]

[a] Plasma Processing Laboratory, Department of Chemical Engineering, McGill University, 3610 University Street, Montréal, Québec H3A 0C5, Canada
[b] Electrochemistry and Corrosion Laboratory, Department of Chemical Engineering, McGill University, 3610 University Street, Montréal, Québec H3A 0C5, Canada

HIGHLIGHTS

- Ni NPs were deposited onto MWCNTs in a single step dry process.
- The electrocatalytic activity of Ni NP/MWCNT in terms of hydrogen evolution is dependent on the NP loading.
- The Ni NP/MWCNT electrocatalysts show a significant increase in electrocatalytic activity relative to a bulk Ni plate.

ARTICLE INFO

Article history:
Received 8 January 2014
Received in revised form
10 May 2014
Accepted 10 May 2014
Available online 20 May 2014

Keywords:
Pulsed laser ablation
Multiwall carbon nanotubes
Ni nanoparticles
Linear Tafel polarization
Electrochemical impedance spectroscopy
Hydrogen evolution reaction

ABSTRACT

Renewable alternative energy sources are required to decrease or eliminate the use of environmentally unfriendly fossil fuels. Hydrogen produced by electrolysis has been identified as one such renewable energy carrier. In the current work, Ni nanoparticle (NP)-*decorated* multiwall carbon nanotube (MWCNT) electrocatalyst cathodes are prepared by a simple two-step procedure. MWCNTs are grown on stainless steel meshes by thermal-chemical vapour deposition (t-CVD) and then decorated with Ni NPs by pulsed laser ablation (PLA). The morphological and electrochemical properties of the produced Ni NP/MWCNT cathodes were characterized through electron microscopy and linear Tafel polarization (LTP)/electrochemical impedance spectroscopy (EIS), respectively. SEM and TEM imaging revealed that the Ni NPs deposited by PLA are on the order of 4 nm in diameter with a narrow size distribution. The LTP measurements showed that the electrocatalytic activity of the Ni NP/MWCNT cathodes towards the hydrogen evolution reaction (HER) is dependent on PLA time and shows a maximum at $t_{PLA} = 40$ min. EIS measurements revealed that the HER response is characterized by a two time constants process representing HER kinetics and adsorption of hydrogen.

1. Introduction

It has been established that energy consumption increases with global development. However, traditional fossil-based fuels may be insufficient to meet the need due to their finite supply. Hydrogen has been identified as a clean energy fuel carrier; as the most abundant element on Earth, hydrogen is truly renewable and has a large energy storage potential [1–3]. For these reasons, hydrogen has been referred to as the "*fuel of the future*".

Electrolysis in alkaline media has been used for a number of years to electrochemically generate hydrogen [4–7]. Electrolysis also offers high purity (near 100%) hydrogen production for a modest energy input [5]. However, alkaline electrolyzers have some disadvantages that must be considered, such as the use of very alkaline electrolyte (30 wt.% KOH), large system size, and large total cell operating potential due to the presence of various ohmic drops in the cell (including those related to the electrode reaction kinetics) [6,8]. Despite these shortcomings, there has been a renewed interest in alkaline electrolysis [9]. The current work addresses the latter issue, and more specifically, it focuses on the improvement of the hydrogen evolution reaction kinetics.

Electrocatalysts (cathodes) for hydrogen generation typically consist of a metal electrode supported on an inert conductive support. The best hydrogen generating metals are noble metals (Pt, Ru, Ir). This is a direct consequence of the intermediate M–H_{ads} bond strength in the hydrogen evolution reaction (HER) [10,11]. In alkaline electrolyzers, non-noble metal electrocatalysts are used to

* Corresponding author. Department of Chemical Engineering, McGill University, 3610 University Street, Montréal, Québec H3A 0C5, Canada.
E-mail address: mark.mcarthur@mail.mcgill.ca (M. McArthur).

http://dx.doi.org/10.1016/j.jpowsour.2014.05.036
0378-7753/

circumvent the use of expensive noble metals. Unfortunately, two major drawbacks are associated with the use of non-noble metal cathodes in alkaline electrolyzers: (i) operation at a large overpotential due to the poor electrocatalytic properties of the cathode material relative to noble metals and (ii) the bulkiness of the system due to the requirement for a large surface area to generate sufficient amounts of hydrogen. Of the non-noble metals, nickel has been identified as a good candidate electrocatalyst material due to its low cost and relatively large electrocatalytic activity [12,13]. Two main approaches for the improvements of the electrocatalytic activity of Ni have been applied: (i) modification of its intrinsic (material-related property) [8,14–16] and (ii) extrinsic (surface area-related property) [14–20] electrocatalytic activities. The current work focuses on (ii).

Numerous attempts have been made to modify the extrinsic factors associated with the HER on Ni electrodes. In a recent study by Lahiri et al., an electrodeposited microporous Ni film was used as a dual-use HER and hydrogen storage (through the formation of nickel hydrides) electrode in an ionic liquid electrolyte [21]. Further, Döner et al. have recently shown that non-noble transition metals (Ni, Co, and their alloy) can be electrodeposited onto carbon felt to produce porous metal coatings on a large area support which yields very effective HER electrocatalysts in alkaline media [22]. For the case of the Ni–Co alloy, a measure of the electrocatalyst's intrinsic electrocatalytic activity was studied as well. Unsupported Ni powders have also been suggested as an alternative to Pt electrocatalysts in electrochemical hydrogen pumps [23]. These Ni nanomaterial studies are not limited to 2D electrodes. Yang et al. have recently reported a 3D electrode material using boron-doped diamond nanowires locally tipped with Ni nanoparticles for generic use as HER and glucose oxidation electrodes in alkaline electrolyte [24]. Clearly, Ni is an attractive alternative for reducing the cost of hydrogen generating technologies.

Much attention has recently been given to nanomaterials for a myriad of applications. One of the first major breakthroughs in nanomaterial synthesis originated from the discovery of carbon nanotubes (CNTs) by Iijima [25]. Since their discovery, CNTs have seen wide-spread use in many fields, including alternative energy, medicine, and nanofluid development, to name but a few [26–28]. Novel CNT synthesis techniques have recently been developed using thermal-chemical vapour deposition (t-CVD) where multiwall CNTs (MWCNTs) are grown in a single step onto a metal supporting catalyst [28,29]. It has been reported that MWCNT synthesis can be done easily, inexpensively, and readily scaled up using t-CVD [28]. In the t-CVD process developed in our laboratory, the MWCNTs form an open 3D matrix onto which other nanomaterials, such as metal electrocatalyst nanoparticles (NPs), can be readily immobilized [30]. The NP-*decorated* MWCNTs show a tremendous increase in active surface area on which an electrochemical reaction can be performed.

There are several techniques currently used to synthesize metal nanoparticles including wet chemistry methods as well as dry methods, including cathodic arc erosion, and pulsed laser ablation (PLA) [30–34]. Of these techniques, PLA has been shown to be very effective at synthesizing highly dispersed streams of metal NPs with small diameters, tight size distributions, and without producing significant amounts of micron-sized particles. These properties are very desirable in terms of high-surface area electrocatalyst materials and as such, PLA has been chosen for NP synthesis in the current work.

In this work, the marriage between nanoparticle and nanotube complement each other to produce high-area Ni NP-decorated MWCNT forests on which HER can occur. However, metal nanoparticle immobilization onto MWCNTs is not a new concept. For example, recent studies have shown that it is possible to combine both using various techniques. Martis et al. were able to synthesize carbon nanotube/Ni nanocrystal composites using electrodeposition [35,36]. However, imaging of the composite readily revealed that the MWCNTs heavily agglomerated and formed a "film" incorporating sparsely distributed Ni particles. It is unknown whether these materials would behave as truly 3D HER electrodes. Further, Zhang et al. have shown that Ni NPs can be immobilized onto MWCNTs by chemical reduction from Ni-containing salt precursors [37]. Others have also shown that it is possible to combine Ni NPs and MWCNTs through chemical reduction [38–40]. Unfortunately, using chemical reduction/electrochemical plating results in either large metal particles or thin Ni films covering the MWCNTs. Both geometries are undesirable for HER; agglomerations of NPs trap evolved hydrogen gas reducing available surface area and the available surface area is not initially maximized, respectively.

What these few examples suggest is that wet chemistry/electrochemistry methods for metal nanoparticle immobilization on MWCNTs are relatively common. However, physical deposition (dry) methods are not encountered as frequently. PLA has been used in the past to immobilize metal nanoparticles on MWCNT surfaces. For example, Mortazavi et al. have synthesized Pd nanoparticle/MWCNT hydrogen storage electrodes in deionized water [41]. It is unclear how much of the MWCNTs were covered with Pd as the MWCNTs were in a fluidized powder form. Because pristine MWCNTs were purchased as a powder, it is unclear what was the degree of MWCNT agglomeration prior to PLA. As a result, it is surmised that only the outer portion of the agglomerates would be covered by nanoparticles. Subsequently, the fabricated hydrogen storage electrodes were dropped onto a graphite plate and dried. It is the authors' opinion that the drying step would cause further agglomeration of the MWCNTs and contribute to a lower overall surface area due to the hydrophobic nature of pristine MWCNTs.

We show that Ni NP/MWCNT electrocatalysts for hydrogen generation can be synthesized easily and efficiently with a great level of control. Using t-CVD and PLA, an effective Ni NP electrocatalyst supported on an open 3D MWCNT matrix grown on an inexpensive porous stainless steel substrate (mesh) was produced in a simple two-step process. The simplicity of the electrode synthesis, the 3D nanostructure of the MWCNTs, and the control of NP deposition (size, absence of agglomeration, etc.) offered by PLA yield marked improvements over (effectively 2D) nanostructured Ni electrocatalysts used in the past. This electrocatalytic nanomaterial offers a marked increase in electrocatalytic activity in the hydrogen evolution reaction (HER) relative to bulk Ni (a 2D Ni plate).

2. Experimental considerations

2.1. MWCNT growth by t-CVD

An established t-CVD technique first developed by Baddour et al. and later modified by Hordy et al. [28,29] was followed to grow MWCNTs for use as electrically-conductive electrocatalyst supports. In this technique, stainless steel (SS) 316 grade mesh discs (400 series, 25 μm grid bar, 1.6 cm dia.; McMaster-Carr, USA) are used as the catalyst/substrate for MWCNT growth. The SS discs are first degreased in acetone for 30 min and then placed in a quartz tube furnace (55 mm i.d.) and heated to 700 °C under flowing Ar (592 ± 5 cm^3 min^{-1}). Acetylene is used as the carbon source and injected into the furnace for 4 min at a constant flow rate of 68 ± 5 cm^3 min^{-1} followed by an isothermal growth step of 30 min at 700 °C under Ar (592 ± 5 cm^3 min^{-1}). Afterwards, the system is allowed to cool down to room temperature (22 °C) before removing the MWCNT-covered SS mesh (MWCNT/SS) electrodes from the

furnace. To establish quantitative information regarding the mass increase of the SS mesh electrodes due to MWCNT growth and carbon absorption, SS mesh electrodes are weighted before and after using a microbalance (Sartorius, USA).

2.2. Ni NP decoration by PLA

Decoration of MWCNT/SS electrodes with Ni NPs was performed in a custom-designed PLA system operating under low pressure (ca. 2.5–3.0 mTorr, He) and at room temperature (ca. 22 °C). NP decoration consists of the sparse deposition of well-dispersed nanoparticles onto a host surface, where the NPs add localized chemical and/or physical properties to the surface. The PLA system consists of an SS vacuum chamber wherein a Ni target (2.54 cm dia., 0.32 cm thickness, 99.9% pure; Kurt J. Lesker Co., USA) is held in place on a computer-controlled linear translation stage to minimize localized target erosion. A frequency-tripled pulsed Nd:YAG laser (Brilliant B10, Quantel, France; 355 nm, 10 Hz, 5 ns pulse duration) is focused on the target surface at an angle of 45°. The resulting laser fluence, 2.36 ± 0.01 J cm^{-2}, is above the minimum ablation threshold. The metal vapour plume produced by the laser pulse expands in the low-pressure background gas, forming NPs by supersaturation of the vapour, and simultaneously imparts momentum to the *in-situ* synthesized NPs for their transport to the collection surface. The MWCNT/SS 316 electrodes are fixed opposite to the target on an adjustable platter and collect well-dispersed Ni NPs. The PLA target-to-electrode separation is 7 cm.

Visual characterization of the Ni NP-decorated MWCNT/SS and bare MWCNT/SS electrodes was conducted using field emission scanning electron microscopy (FE-SEM; Hitachi S-4700; 2.0 keV electron acceleration energy) and transmission electron microscopy (TEM; Phillips CM200, FEI Co., USA). Henceforth, the Ni NP-decorated MWCNT/SS electrodes will be referred with their respective PLA time (in min) followed by Ni/MWCNT, e.g., 30-Ni/MWCNT for 30 min of PLA.

2.3. Electrochemical characterization

The electrocatalytic activity of electrodes towards hydrogen evolution was investigated using two standard electrochemical techniques: (i) linear Tafel polarization (LTP) and (ii) electrochemical impedance spectroscopy (EIS). Both techniques were performed in a typical 3-electrode electrochemical cell in 1 M KOH electrolyte (pH 14, 90% assay; Sigma–Aldrich, USA). The Ni/MWCNT working electrode was held in place using a PTFE holder (flat specimen holder, Princeton Applied Research, USA). The cathode area exposed to the electrolyte was 0.785 cm^2. In order to prevent reduction of oxygen formed at the graphite counter electrode, and thus its interference with the HER at the working electrode, the counter electrode was separated from the main electrochemical cell compartment by a glass frit (Ace Glass, Inc., USA). A saturated calomel electrode (SCE) (Accumet electrode, Fisher Scientific, USA) was used as the reference electrode. LTP and EIS measurements were performed on a computer-controlled combination potentiostat/galvanostat/frequency response analyzer (Autolab PGSTAT30, Metrohm, NL) using Autolab GPES and FRA software packages (v. 4.9; Metrohm, NL).

Prior to electrochemical measurements, the Ni/MWCNT electrode was conditioned for 2 h at a potential of −1.35 V vs SCE (i.e., an HER overpotential (η) of −0.29 V) to remove any native Ni-oxide

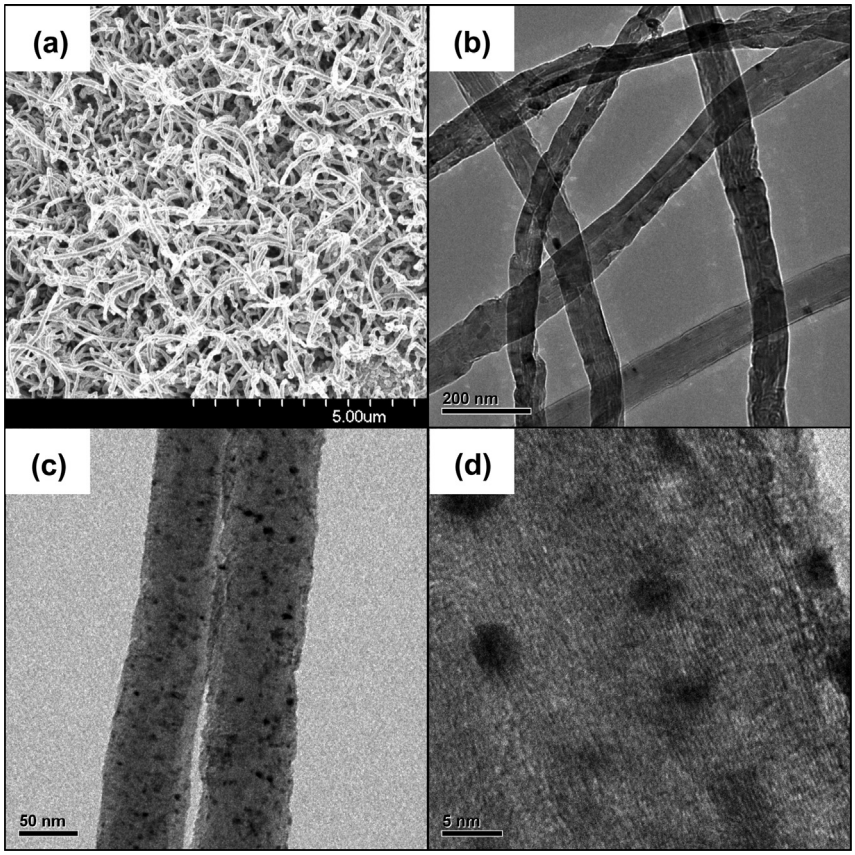

Fig. 1. Micrographs displaying the nanostructured morphology of the Ni/MWCNT electrodes for various PLA times prior to electrochemical testing. (a) SEM image of Ni/MWCNT for 20 min PLA time, (b) TEM image of Ni/MWCNT for 0 min PLA time (control), TEM image of Ni/MWCNT for (c) 20 min PLA time, and (d) higher magnification of (c).

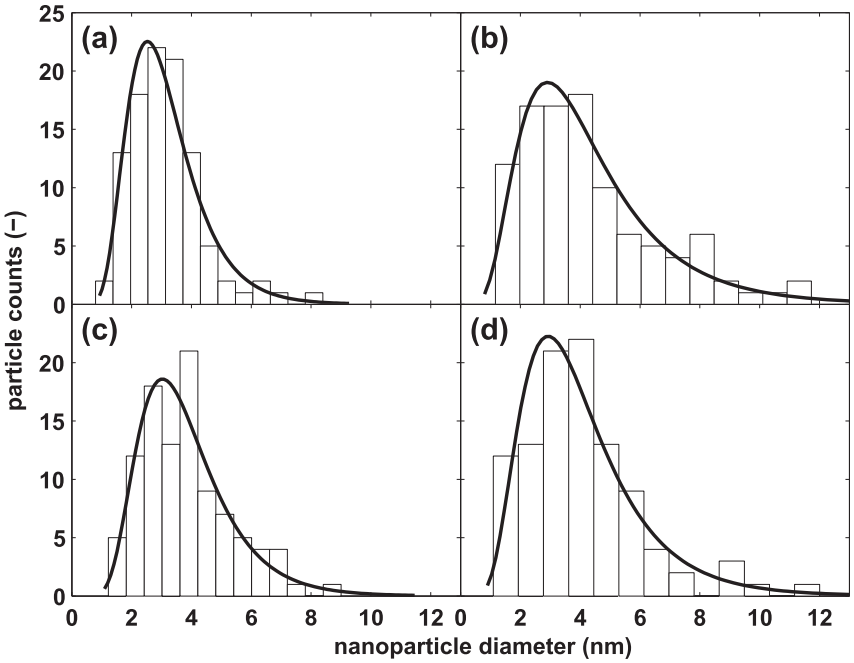

Fig. 2. Ni nanoparticle size distributions histograms for: (a) 20 min, (b) 30 min, (c) 40 min, and (d) 50 min PLA times. 13 equally spaced bins were chosen for each respective data set. The solid curve represents the best-fit log-normal distribution. Sample size: 101 nanoparticles.

present on the electrocatalyst surface. Linear sweep voltammetry was performed for LTP measurements between $0.06\,V \leq \eta \leq -0.34\,V$ at a sweep rate (s.r.) of 1 mV s^{-1}. The LTP data were corrected for the iR-drop due to the resistance of the electrolyte between the working and reference electrode. EIS measurements were performed between $-0.04\,V \leq \eta \leq -0.44\,V$ in overpotential steps of 0.05 V. The frequency range used was between 50 mHz and 50 kHz with an AC voltage amplitude of 10 mV. However, for overpotentials $\eta > -0.19\,V$, phase and amplitude information could not be obtained for the majority of the electrocatalysts studied. This is due to a high degree of noise attributed to extreme H_2 gas generation at the electrode surface that resulted in accumulation of H_2 bubbles between MWCNTs and the subsequent gas release after a certain pressure was attained. As a result of this noise, only EIS spectra for 40-Ni/MWCNT are presented in the lower potential region (this will be discussed further in subsequent sections).

3. Results and discussion

3.1. Electrocatalyst morphology

Fig. 1a–d shows electron micrographs clearly revealing the morphology of the Ni NP/MWCNT electrocatalyst cathodes. Fig. 1a shows a low-resolution SEM micrograph of a 20-Ni/MWCNT electrode. The micrograph reveals a dense, yet open 3D network of a large surface area. Nominal MWCNT diameters fell in the range of 60–100 nm. Micrographs b and c are high-resolution TEM images of Ni/MWCNT electrocatalysts for 0 and 20 min of PLA time, respectively. Micrograph d shows a high-magnification TEM image of micrograph c to further describe the Ni NP sizes. As expected, the TEM of 0-Ni/MWCNT electrodes show smooth, rather featureless MWCNTs. As is consistent with Fig. 1a, the TEM in Fig. 1b shows that the MWCNTs are ca. 60–100 nm in diameter. Contrary to the SEM image in Fig. 1a, the TEM images (c, d) reveal the presence of individual Ni NPs. It is observed that the NPs are well dispersed along the MWCNTs. Good dispersion of NPs is a common feature characteristic of the PLA technique.

Fig. 2a–d shows the Ni NPs size distributions for 20, 30, 40, and 50 min of PLA time, respectively. In each case, 101 NPs were randomly sampled from several TEM images (additional images not shown). The mean NP diameter for each of the t_{PLA}'s is ca. 4 nm. As hypothesized, the small NP size allows for tremendous electrochemically active sites on which the HER can occur. Due to the very nature of the PLA technique, and as documented in Fig. 1, Ni NPs do not agglomerate on the MWCNT surfaces which maximizes the electrochemically-active area and, most likely, the surface energy (and thus electrocatalytic activity) for H_2 production. As is consistent with NP formation, the size distribution is log-normal [42–44]. This is emphasized by the fitted log-normal distribution curves in Fig. 2a–d. Table 1 briefly summarizes log-normal mean ($\mu_{lg\text{-}n}$) and variance ($(\sigma^2)_{lg\text{-}n}$) for each of the PLA times. As stated earlier, an advantage of PLA for the synthesis of NPs is the high degree of control (NP narrow and narrow size distribution). PLA time has no significant effect on the individual NP size distribution. These results yield evidence that NP formation occurs in flight prior to substrate attachment, and not from a surface growth from a stream of metallic vapours as it is commonly observed in pulsed laser deposition where the chamber pressure is kept at much lower values. If the NPs were to form on the MWCNTs, we would expect the particle size to grow with ablation time. It is also noteworthy that as PLA time increases, the NP coverage increases without the formation of large agglomerates within the PLA time interval employed, thus evidencing that significant coverage can be achieved before NP *piling* or agglomeration starts to occur.

Table 1
Summary of mean and variance of Ni NP particle size distributions using the log-normal distributions of Fig. 2 for PLA times of 20, 30, 40, and 50 min from several TEM images. Sample size = 101 NPs.

t_{PLA} (min)	$\mu_{lg\text{-}n}$ (nm)	$(\sigma^2)_{lg\text{-}n}$
20	3.2	1.6
30	4.2	5.8
40	3.8	2.4
50	4.1	4.0

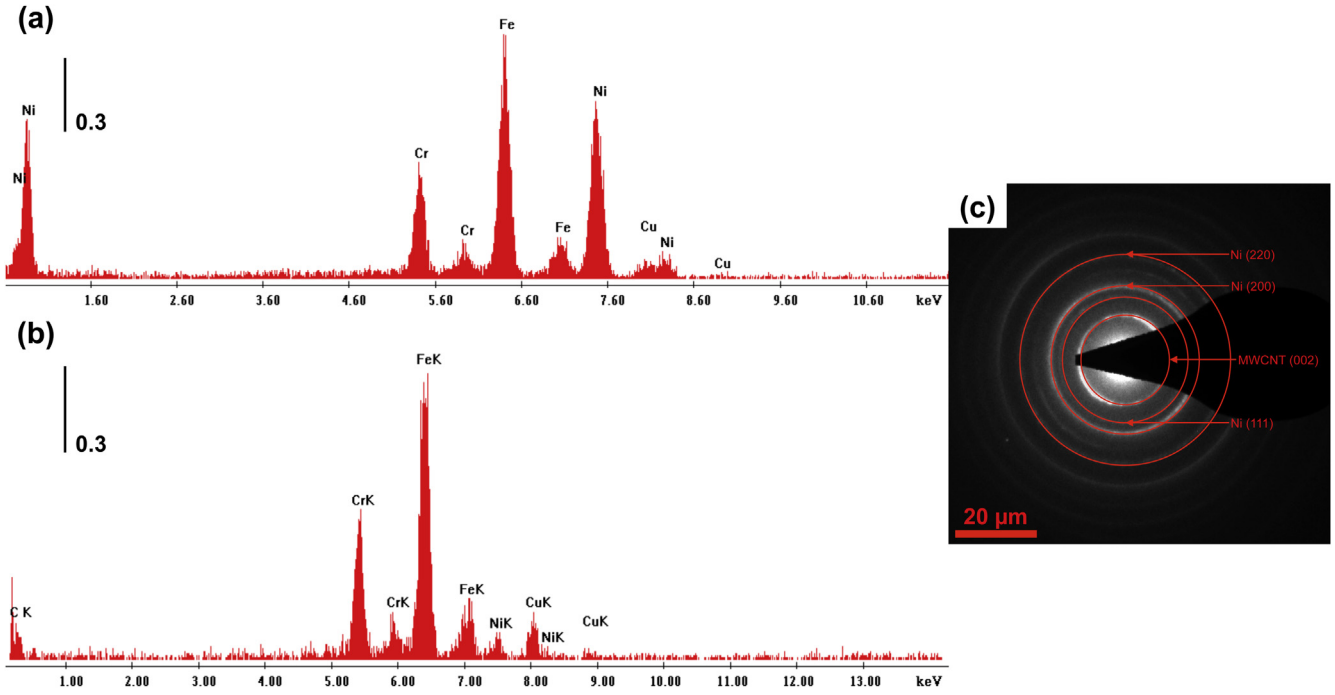

Fig. 3. Energy-dispersive spectroscopy (EDS) spectra for a Ni/MWCNT electrocatalyst (a) and a fresh MWCNT electrode (b) and selected area electron diffraction (SAED) pattern (c) of the Ni/MWCNT electrocatalyst from TEM measurements. Elemental identifiers are given above the respective peaks in (a) and (b). Selected rings are shown in (c).

Fig. 3a–c shows the energy-dispersive spectroscopy (EDS) spectra of the Ni/MWCNT cathode (a), the fresh MWCNT electrode (b) and selected area electron diffraction (SAED) pattern of the Ni/MWCNT cathode (c) from TEM measurements, respectively. The presence of several metals was observed in EDS. The majority of these metals can be attributed to sources external to the electrocatalyst; Cu peaks are from the TEM substrate holder, whereas Fe and Cr are attributed to the underlying SS mesh and/or the alloy used in the TEM sample holder. The Ni peaks come from the combined effect of Ni NPs and the SS mesh. However, a control experiment on pure MWCNTs (no Ni NPs) deposited on SS mesh (Fig. 3b) demonstrated that the Ni peaks are significantly smaller than those in Fig. 3a, indicating that the latter are predominantly the response of Ni NPs, not the underlying SS substrate/TEM sample holder. In Fig. 3c (SAED), characteristic continuous ring patterns are observed. These rings describe the electron interactions with the Ni NPs as well as the MWCNTs. The continuous rings confirm that the NPs are very small (less than 10 nm in size). Otherwise, discrete points would be observed. Several rings have been highlighted using red circles. These circles correspond to the ordered MWCNT (002), Ni (111), Ni (200), and Ni (220) reflections. These reflections show that the electrocatalyst has a nanocrystalline structure.

Fig. 4 compares the Ni NP/MWCNT cathode mass increase for each synthesis step and for various PLA times. As expected, the Ni NP loading, i.e., Ni NP mass, increases roughly linearly with PLA time. It should be noted that the mass of the SS mesh after t-CVD overestimates the mass of the MWCNTs themselves. The reason for the carbon and MWCNT mass discrepancy is outside of the scope of the current work. Suffice it to say that carbon from the process gas absorbs into the bulk SS without MWCNT formation and hence, a relatively large mass increase is observed [28,45]. As such, the actual MWCNT mass roughly follows the mass of the SS mesh, i.e., mass of MWCNTs is 4 mg per 1000 mg of SS mesh (with 20% uncertainty). For further information regarding MWCNT mass by t-CVD and the computation to determine the actual MWCNT mass, the reader is referred to Refs. [28,45].

3.2. Electrochemical characterization

3.2.1. LTP measurements

Fig. 5 shows representative HER Tafel curves for a 2D Ni plate (a) and Ni/MWCNT cathodes with PLA times of 20 min (b), 30 min (c), 40 min (d), and 50 min (e). Briefly, the applied overpotential presented on the abscissa represents the driving force for the electron transfer in the HER, i.e., the input energy, while the current density presented on the ordinate represents the corresponding HER kinetics, i.e., the amount of H_2 produced. Since the HER is an electron

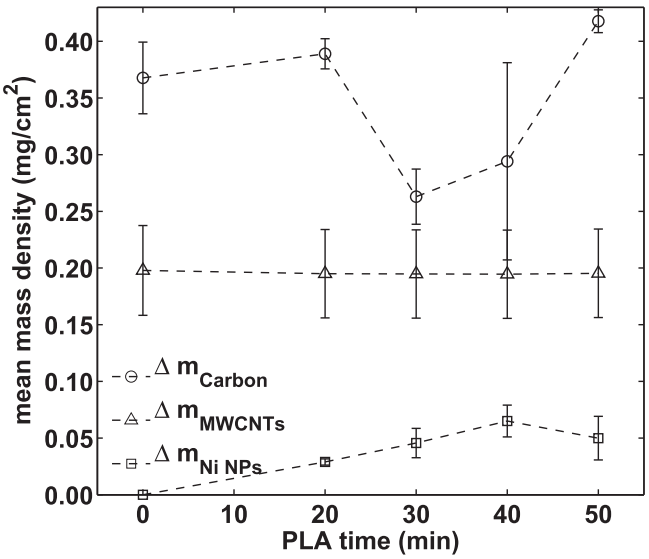

Fig. 4. Mean mass density data for the Ni/MWCNT electrocatalyst cathodes taken during their synthesis for the various PLA times. Error bars for the change in mass due to carbon input and change in mass due to Ni NP decoration indicate the standard deviation. The error bars for the change in mass due to MWCNTs is a constant 20%. The connecting lines presented are meant to be a guide for the eye only.

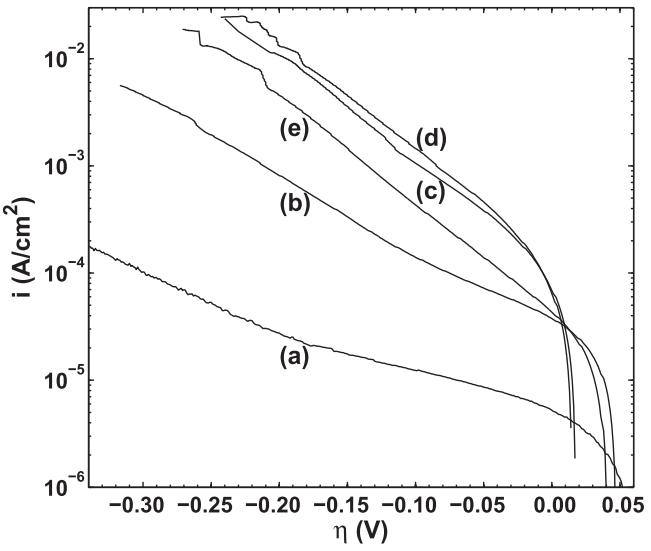

Fig. 5. Linear Tafel polarization curves for 2D Ni plate and various Ni/MWCNT electrocatalyst cathodes recorded in the potential region of hydrogen generation in 1.0 M KOH electrolyte (solid curves). (a) 2D bulk Ni plate (control), (b) 20-Ni/MWCNT, (c) 30-Ni/MWCNT, (d) 40-Ni/MWCNT, and (e) 50-Ni/MWCNT.

transfer-controlled reaction, the presented Tafel curves are linear in the semi-log presentation (Fig. 5). Consequently, as overpotential increases to more negative values, the driving force for electron transfer increases, and thus the HER kinetics/amount of H_2 produced. Accordingly, an electrocatalyst with a larger current density measured at a constant potential, is desired.

Curve (a) in Fig. 5 evidences that the Ni plate (control sample) offers the lowest electrocatalytic activity in the HER among the investigated electrodes. Curve (b) represents the response of a 20-Ni/MWCNT electrode. It is known that carbonaceous materials, including MWCNTs, have very large HER overpotentials and are thus relatively inert to the HER in the overpotential region investigated. Thus, one can conclude that the overpotential-dependant increase in current on the 20-Ni/MWCNT electrode (curve (b)) is due to the presence of Ni NPs on the MWCNT surface. Interestingly, curve (b) is ca. 1.5 orders of magnitude higher than the control response (curve (a)) despite the fact that PLA deposition of Ni NPs on MWCNTs was done for only 20 min. This indicates that even a short Ni PLA time is sufficient to yield a substantially increased electrocatalytic activity of Ni/MWCNT electrodes in comparison to the control Ni plate.

Curves (c)–(e) in Fig. 5 display even higher current densities than curve (b), demonstrating that the electrocatalytic activity of Ni/MWCNT electrocatalysts further increases in order 50 < 30 < 40 min for PLA time. Interestingly, the PLA time appears to play a large role in the observed current density. Taking into account that the NP size distribution is relatively independent on the PLA time (Fig. 2), and that with an increase in PLA time, the amount of Ni NPs on the MWCNTs also increases (Fig. 4), it seems that the corresponding surface area available for the HER, i.e., the surface coverage by Ni NPs, also increases in parallel. This, in turn, results in an apparent increase in catalytic activity of Ni/MWCNT, as demonstrated in Fig. 5. A maximum activity is obtained for 40-Ni/MWCNT (curve (d)), but as the PLA time continues to increase to 50 min (50-Ni/MWCNT), the current density decreases. This effect is thought to be due to a reduction in the electroactive surface area due to the agglomeration of Ni NPs on the MWCNT surface.

In order to properly evaluate the results shown in Fig. 5, it is important to briefly discuss what others have attained for Ni NP- and Ni-supported carbon electrocatalysts. For example, Döner et al. [22] have reported on electrodeposited Ni supported carbon felt HER electrocatalysts in 1 M KOH. However, these electrocatalysts showed an inferior electrocatalytic activity of roughly 1.5 orders of magnitude (at $\eta = -0.3$ V) than our own 40-Ni/MWCNT electrocatalyst. Similarly, a study by Kang et al. [46] on Ni NP-supported mesoporous carbon electrocatalysts in 1 M NaOH showed an electrocatalytic activity approximately 4 orders of magnitude lower than our own (at $\eta = -0.3$ V). Finally, Yang et al. [24] have reported on Ni NP-tipped diamond nanowires in 1 M NaOH. These electrodes again demonstrated an electrocatalytic activity roughly 2.5 orders of magnitude lower than our own (at $\eta = -0.3$ V). In addition, the Tafel slope for the HER employing our 40-Ni/MWCNT catalyst was lower than that of the other Ni-supported carbon electrocatalysts described above. Comparing these recent studies with our own, it is clear that the 40-Ni/MWCNT electrocatalyst prepared by PLA is a marked improvement over what has been reported previously.

In order to quantify the electrochemical activity of all the HER electrocatalysts presented in Fig. 5, it is useful to examine the corresponding electrocatalytic activity at a specified overpotential. Thus, Fig. 6 compares the relative electrocatalytic activity of the Ni/MWCNT cathodes to a 2D bulk Ni plate cathode from LTP measurements, at overpotential −0.22 V. The data were obtained by normalizing the current density of the Ni/MWCNT cathodes to that of the 2D bulk Ni cathode. Fig. 6 demonstrates that the electrocatalytic activity of the cathodes at −0.22 V increases with PLA time to a maximum at 40 min, where the 40-Ni/MWCNT cathode showed the HER electrocatalytic activity of ca. 605 times higher than that shown by the 2D Ni plate. However, prolonging the PLA time past 40 min results in a decrease in the electrocatalytic activity of 50-Ni/MWCNT. Nevertheless, this electrode is still significantly more active than the control surface (2D Ni plate). In summary, Fig. 6 demonstrates that Ni/MWCNT 3D electrocatalysts perform significantly better in the HER than a control 2D Ni cathode.

From the Tafel curves, one can extract several comparative pieces of information regarding the electrocatalytic activity of the Ni NP/MWCNT cathodes, including the cathodic Tafel slope, b_C (mV dec^{-1}), the electron transfer coefficient, α, and the exchange current density, i_0 (A cm^{-2}). It has been shown that the Tafel slope yields mechanistic information about the HER. From models of the HER [47–49], if the Volmer, Tafel, or Heyrovsky reaction is rate-

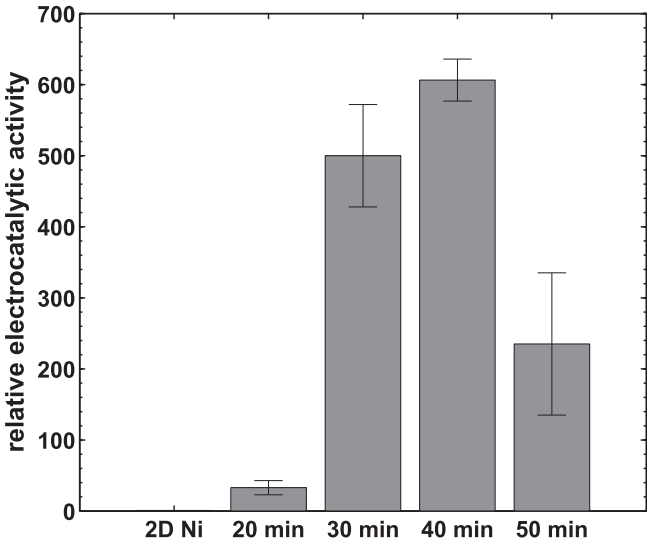

Fig. 6. Comparison of electrocatalytic activity of the Ni/MWCNT electrocatalyst cathodes relative to a 2D bulk Ni plate. Time along the abscissa indicates the PLA time. Data used for comparison are from LTP measurements at an overpotential of −0.24 V. Presented error is from standard deviation of the mean.

Table 2
Tafel parameters (Tafel slope, exchange current density, transfer coefficient, and current density at −0.22 V) for the various PLA times compared to the bulk 2D Ni plate cathode. Presented errors are standard deviations of the mean.

t_{PLA} (min)	b_C (mV dec^{-1})	i_0 (A cm^{-2})	α	i at −0.22 V (A cm^{-2})
20	−129 ± 19	(8 ± 3) × 10^{-5}	0.46 ± 0.07	(1.0 ± 0.3) × 10^{-3}
30	−104 ± 5	(9 ± 4) × 10^{-5}	0.56 ± 0.03	(11 ± 5) × 10^{-3}
40	−102 ± 3	(11 ± 7) × 10^{-5}	0.57 ± 0.02	(20 ± 3) × 10^{-3}
50	−130 ± 30	(4.4 ± 0.5) × 10^{-5}	0.5 ± 0.1	(5 ± 2) × 10^{-3}
Bulk 2D Ni	−284 ± 30	(0.6 ± 0.1) × 10^{-5}	0.21 ± 0.04	(0.045 ± 0.007) × 10^{-3}

determining, b_C values of −116, −30, and −40 mV dec^{-1} are expected, respectively at 20 °C. Fig. 5 shows that two different behaviours, with respect to the Tafel slope, are evident: electrocatalyst (a) has a relatively large Tafel slope, −284 mV dec^{-1} in the lower overpotential region and −170 mV dec^{-1} in the upper overpotential region, while electrocatalysts (b)–(e) share relatively low Tafel slopes, ranging from −130 mV dec^{-1} to −102 mV dec^{-1} (Table 2). These values are consistent with previous works done on the HER on Ni [50–56]. Hence, it is suggested that the Volmer step is rate-determining for the HER on all electrocatalysts, i.e., that the adsorption of H^+ onto the active Ni NP sites is a slow step in the HER. In addition, a smaller Tafel slope is preferential since a smaller change in electrode overpotential results in a larger increase in HER current, and thus faster hydrogen gas production.

From the Tafel slopes in Fig. 5, the electron transfer coefficient was next estimated through $\alpha = (-2.3RT)/(b_C nF)$, where R is the gas constant (8.314 J mol^{-1} K^{-1}), n is the number of electrons transferred in the reaction, T is temperature, and F is Faraday's constant (96,485 C mol^{-1}). The electron transfer coefficient is useful for comparing the efficacy of the Ni/MWCNT cathodes and, it is desirable to have a large electron transfer coefficient value. Table 2 summarizes these above-mentioned quantities. As it can be seen, the four Ni/MWCNT cathodes have a significantly higher transfer coefficient value than the control 2D Ni plate. Further, with an increase in PLA time, the transfer coefficient value increases and reaches a maximum for 40-Ni/MWCNT, followed by a slight decrease. This trend resembles the trend in electrocatalytic activity shown in Figs. 5 and 6, again evidencing that the 40-Ni/MWCNT cathode is the most active in the HER among the investigated materials. A similar trend was also obtained by the analysis of exchange current density, i_0, presented in Table 2. In conclusion, all the analysis parameters presented in Table 2, which are related to the Tafel curves in Fig. 5, display the same trend and clearly evidence that the 40-Ni/MWCNT cathode is the most active in the HER among the investigated materials, not only in terms of its extrinsic properties (i_0 and $i_{-0.22\ V}$) but also intrinsic properties (b_C and α).

3.2.2. EIS measurements

Electrochemical impedance spectroscopy measurements were performed to corroborate the LTP results and obtain information regarding the kinetics of the HER at the cathode/electrolyte interface. Fig. 7a and b shows typical Nyquist and Bode plots, respectively, recorded at different overpotentials on the 40-Ni/MWCNT cathode. In Fig. 7a, the impedance semicircle decreases in diameter with an increase in overpotential, indicating a decrease in the ohmic (real) component of the resistance related, in the first approximation, to the HER reaction kinetics. Taking into account Ohm's law, this is in accordance with the LTP results presented in Fig. 5, curve (e).

From the phase data presented in the Bode plot (Fig. 7b), a broad, asymmetrical peak is observed near 2–8 Hz, especially on the spectra recorded at lower overpotentials. The asymmetry of the phase data, most notably visible at low overpotentials, suggests that the HER mechanism and kinetics on the 40-Ni/MWCNT catalyst surface is governed by a two time constants response. This behaviour is consistent with other work on the HER on Ni electrodes [8,31,32,57]. Thus, in order to describe the physical meaning of the EIS response in Fig. 7, a two-time-constant electrical equivalent circuit (EEC) model was used to model the experimental data employing nonlinear least-squares fitting (NLLS). The inset of Fig. 7a shows the electrochemical equivalent circuit (EEC) proposed to model the EIS data in this work. The EEC consists of two parallel capacitance-resistance time constants, represented by the constant phase element ($CPE_{(1,2)}$; F s^{n-1} cm^{-2}) − resistance ($R_{(1,2)}$; Ω cm^2) combinations in series with an electrolyte resistance (R_{el}). The use of a CPE instead of pure capacitance yielded a better agreement to the data, and it was justified by the existence of relaxation times

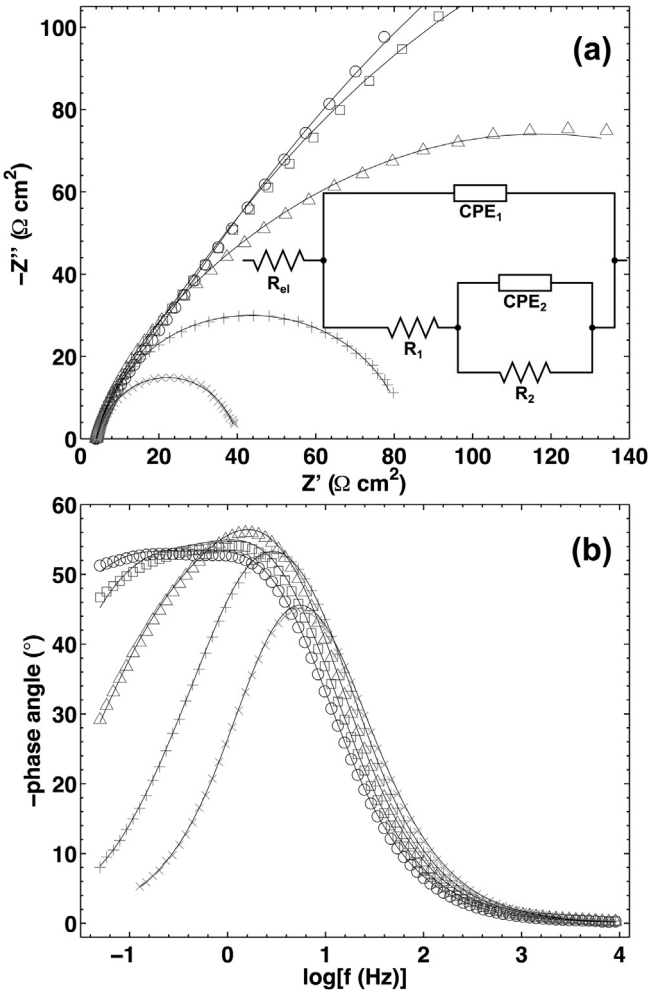

Fig. 7. Nyquist (a) and Bode (b) plots showing the EIS response of a 40-Ni/MWCNT cathode at various overpotentials. Symbols are experimental data and solid curves are the best-fit NLLS model to the 2-time constant EEC presented in the inset. (○) −0.04 V, (□) −0.09 V, (△) −0.14 V, (+) −0.19 V, (×) −0.24 V.

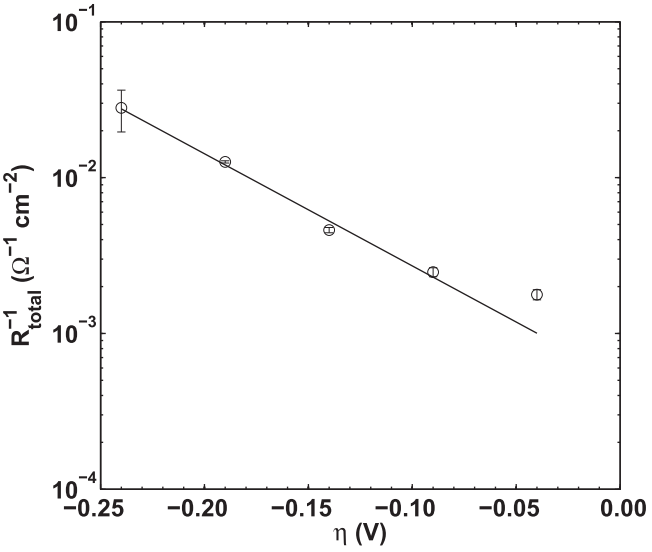

Fig. 8. A pseudo-Tafel plot of total inverse resistance extracted from the EIS fitting parameters with overpotential.

resulting from surface inhomogeneities present at the nano-level on the Ni/MWCNT surfaces [58–64]. The proposed EEC is a modified version of that put forward by Armstrong and Henderson [65] and has been used to successfully describe the response of the HER on porous and smooth electrodes [19,66–69]. The literature suggests that the time constants in the EEC can be related to the kinetics of the HER: the first time constant, CPE_1–R_1, is related to the hydrogen adsorption and the second time constant, CPE_2-R_2, is related to the charge transfer kinetics. In Fig. 7, a fit of the proposed EEC is shown as solid curves. It should be noted that the matched curves show excellent agreement with experimental data (symbols), evidencing that the proposed EEC is suitable for describing the EIS response in Fig. 7.

LTP and EIS are two very different measurement techniques (DC vs AC measurements, respectively). However, both techniques can provide information on the reaction kinetics, which could be taken for comparative/validation purposes. Namely, a dependence of an inverse of the sum of two EIS resistances $(R_1 + R_2)^{-1}$, on overpotential can be compared to the current density behaviour in Fig. 5. Thus, a pseudo-Tafel approach was taken to qualitatively connect the two techniques through the use of Ohm's law. Fig. 8 displays the pseudo-Tafel dependence of the inverse series resistances on overpotential from NLLS EIS modelling. Here, $(R_{total})^{-1}$ represents the total contributions of the inverse series resistances $(R_1 + R_2)^{-1}$. It can be seen that the presented behaviour is linear, which is in agreement with Tafelian behaviour. The corresponding Tafel slope is 139 mV dec^{-1}, which is in the range of what is expected for the HER on Ni and further confirms that the Volmer (hydrogen adsorption) step in the HER is rate determining.

4. Conclusions

A two-step method is presented to prepare heterogeneous electrocatalyst nanomaterials for use as HER cathodes. The benefits of using the t-CVD/PLA technique to synthesize Ni NP/MWCNT cathodes are numerous including a high degree of control of the NP size and size distributions, extent of NP decoration, and the avoidance of NP agglomeration. From LTP electrochemical measurements, it was determined that the electrocatalytic activity of Ni NP/MWCNT cathodes in the HER reaction increases with pulsed laser ablation time up to 40 min, followed by activity decrease. The increasing trend can be related to the increase in electrode surface coverage by Ni NPs, while the decrease in activity can be related to agglomeration of NPs on the surface, and thus to a decrease in the Ni NPs surface area exposed to the electrolyte. The EIS measurements on Ni/MWCNT cathodes revealed that the HER undergoes a two time-constants mechanism representative of the charge transfer kinetics hydrogen adsorption. To the best of the authors' knowledge, the work described illustrates a first for Ni/MWCNT electrocatalysts synthesized using PLA and our own in-house t-CVD technique for the HER in alkaline electrolyte.

Acknowledgements

The authors gratefully acknowledge the financial support provided by NSERC, the Fonds de recherche du Québec – Nature et technologies (FRQNT), and McGill University through the McGill Engineering Doctoral Award (MEDA) program.

References

[1] P. Kruger, Int. J. Hydrogen Energy 25 (2000) 395.
[2] S. Dunn, Int. J. Hydrogen Energy 27 (2002) 235.
[3] T. Hijikata, Int. J. Hydrogen Energy 27 (2002) 115.
[4] P. Barbaro, C. Bianchini (Eds.), Catalysis for Sustainable Energy Production, 2009.
[5] H. Wendt, G. Kreysa, Electrochemical Engineering: Science and Technology in Chemical and Other Industries, Springer, 1999.
[6] National Research Council (U.S.). Committee on Assessment of Resource Needs for Fuel Cell and Hydrogen Technologies, Transitions to Alternative Transportation Technologies a Focus on Hydrogen, National Academies Press, Washington, D.C., 2008.
[7] C.A. Grimes, O.K. Varghese, S. Ranjan, Light, Water, Hydrogen the Solar Generation of Hydrogen by Water Photoelectrolysis, Springer, New York, 2007.
[8] E. Navarro-Flores, Z. Chong, S. Omanović, J. Mol. Catal. A Chem. 226 (2005) 179.
[9] R. Subbaraman, D. Tripkovic, D. Strmcnik, K.-C. Chang, M. Uchimura, A.P. Paulikas, V. Stamenkovic, N.M. Markovic, Science 334 (2011) 1256.
[10] S. Trasatti, J. Electroanal. Chem. Interfacial Electrochem. 39 (1972) 163.
[11] R. Parsons, Trans. Faraday Soc. 54 (1958) 1053.
[12] J. Greeley, M. Mavrikakis, Nat. Mater. 3 (2004) 810.
[13] J. Greeley, T.F. Jaramillo, J. Bonde, I. Chorkendorff, J.K. Nørskov, Nat. Mater. 5 (2006) 909.
[14] L. Chen, J. Electrochem. Soc. 138 (1991) 3321.
[15] P. Los, A. Rami, A. Lasia, J. Appl. Electrochem. 23 (1993).
[16] C. Hitz, A. Lasia, J. Electroanal. Chem. 500 (2001) 213.
[17] M. Metikoš-Huković, A. Jukić, Electrochim. Acta 45 (2000) 4159.
[18] R. Shervedani, A. Lasia, J. Appl. Electrochem. 29 (1999) 979.
[19] R. Šimpraga, G. Tremiliosi-Filho, S.Y. Qian, B.E. Conway, J. Electroanal. Chem. 424 (1997) 141.
[20] S. Tanaka, N. Hirose, T. Tanaki, Int. J. Hydrogen Energy 25 (2000) 481.
[21] A. Lahiri, R. Das, R.G. Reddy, J. Power Sources 195 (2010) 1688.
[22] A. Döner, İ. Karcı, G. Kardaş, Int. J. Hydrogen Energy 37 (2012) 9470.
[23] A.B. Papandrew, T.A. Zawodzinski Jr., J. Power Sources 245 (2014) 171.
[24] N. Yang, W. Smirnov, C.E. Nebel, Electrochem. Commun. 27 (2013) 89.
[25] S. Iijima, Nature 354 (1991) 56.
[26] J. Ma, F. Yu, Z. Wen, M. Yang, H. Zhou, C. Li, L. Jin, L. Zhou, L. Chen, Z. Yuan, J. Chen, Dalton Trans. 42 (2013) 1356.
[27] S. Peretz, O. Regev, Curr. Opin. Colloid Interface Sci. 17 (2012) 360.
[28] N. Hordy, S. Coulombe, J.-L. Meunier, Plasma Processes Polym. 10 (2013) 110.
[29] C.E. Baddour, F. Fadlallah, D. Nasuhoglu, R. Mitra, L. Vandsburger, J.-L. Meunier, Carbon 47 (2009) 313.
[30] L. Rao, N.K. Reddy, S. Coulombe, J.-L. Meunier, R.J. Munz, J. Nanopart. Res. 9 (2006) 689.
[31] A. Damian, S. Omanović, J. Power Sources 158 (2006) 464.
[32] E. Navarro-Flores, S. Omanović, J. Mol. Catal. A Chem. 242 (2005) 182.
[33] S. Amoruso, G. Ausanio, A.C. Barone, R. Bruzzese, C. Campana, X. Wang, Appl. Surf. Sci. 254 (2007) 1012.
[34] G. Ausanio, S. Amoruso, A.C. Barone, R. Bruzzese, V. Iannotti, L. Lanotte, M. Vitiello, Appl. Surf. Sci. 252 (2006) 4678.
[35] P. Martis, V.S. Dilimon, J. Delhalle, Z. Mekhalif, Mater. Chem. Phys. 128 (2011) 133.
[36] P. Martis, B.R. Venugopal, J. Delhalle, Z. Mekhalif, J. Solid State Chem. 184 (2011) 1245.
[37] W. Zhang, X. Zhang, L. Zhang, G. Chen, Sens. Actuators B 192 (2014) 459.
[38] F. Zhang, S.H. Qi, Y. Zhang, J. Thermoplast. Compos. Mater. 26 (2013) 1287.
[39] Y. Zhang, S. Qi, F. Zhang, Mater. Res. Bull. 47 (2012) 3743.
[40] D. Yang, H. Xu, J. Wang, Y. Wu, J. Appl. Polym. Sci. 130 (2013) 3746.
[41] S.Z. Mortazavi, P. Parvin, A. Reyhani, R. Malekfar, S. Mirershadi, RSC Adv. 3 (2013) 1397.

[42] C.G. Granqvist, R.A. Buhrman, J. Appl. Phys. 47 (1976) 2200.
[43] L.B. Kiss, J. Söderlund, G.A. Niklasson, C.G. Granqvist, Nanotechnology 10 (1999) 25.
[44] D. Amans, C. Malaterre, M. Diouf, C. Mancini, F. Chaput, G. Ledoux, G. Breton, Y. Guillin, C. Dujardin, K. Masenelli-Varlot, P. Perriat, J. Phys. Chem. C 115 (2011) 5131.
[45] N. Hordy, Direct Growth of Carbon Nanotubes from Stainless Steel Grids and Plasma Functionalization for Poly(Vinyl Alcohol) Composite Production, MEng, McGill University, 2011.
[46] L. Kang, R.-T. Wang, L.-B. Kong, H. Li, J. Zhang, Y.-C. Luo, Mater. Lett. 64 (2010) 2064.
[47] Southampton Electrochemistry Group, Instrumental Methods in Electrochemistry, Halsted Press, New York, 1985.
[48] E. Ndzebet, O. Savadogo, Int. J. Hydrogen Energy 20 (1995) 635.
[49] B. Børresen, G. Hagen, R. Tunold1, Electrochim. Acta 47 (2002) 1819.
[50] M.A. Domínguez-Crespo, A.M. Torres-Huerta, B. Brachetti-Sibaja, A. Flores-Vela, Int. J. Hydrogen Energy 36 (2011) 135.
[51] C.A. Marozzi, A.C. Chialvo, Electrochim. Acta 46 (2001) 861.
[52] A. Rami, A. Lasia, J. Appl. Electrochem. 22 (1992) 376.
[53] N. Krstajic, S. Trasatti, J. Appl. Electrochem. 28 (1998) 1291.
[54] A. Metikos-Hukovic, Z. Grubac, N. Radic, A. Tonejc, J. Mol. Catal. A Chem. 249 (2006) 172.
[55] M.A. Dominquez-Crespo, E. Ramirez-Meneses, V. Montiel-Palma, A.M. Torres Huerta, H. Dorantes Rosales, Int. J. Hydrogen Energy 34 (2009) 1664.
[56] A. Lasia, A. Rami, J. Electroanal. Chem. 294 (1990) 123.
[57] Z. Bou-Saleh, S. Omanović, J. Nanosci. Nanotechnol. 9 (2009) 2469.
[58] S. Omanovic, S.G. Roscoe, Langmuir 15 (1999) 8315.
[59] S. Omanovic, S.G. Roscoe, J. Colloid Interface Sci. 227 (2000) 452.
[60] M. Kramer, M. Tomkiewicz, J. Electrochem. Soc. 131 (1984) 1283.
[61] S. Liu, Phys. Rev. Lett. 55 (1985) 529.
[62] Z. Kerner, T. Pajkossy, Electrochim. Acta 46 (2000) 207.
[63] T. Pajkossy, J. Electroanal. Chem. 364 (1994) 111.
[64] S. Omanovic, M. Metikos-Hukovic, Thin Solid Films 266 (1995) 31.
[65] R.D. Armstrong, M. Henderson, J. Electroanal. Chem. 39 (1972) 81.
[66] E.B. Castro, M.J. Giz, E.R. Gonzalez, J.R. Vilche, Electrochim. Acta 42 (1997) 951.
[67] F. Rosalbino, G. Borzone, E. Arigelini, R. Raggio, Electrochim. Acta 48 (2003) 3939.
[68] J.M. Jaksic, M.V. Vojnovic, N.V. Krstajic, Electrochim. Acta 45 (2000) 4151.
[69] L. Birry, A. Lasia, J. Appl. Electrochem. 34 (2004) 735.